Article

Characterizing Rain Cells as Measured by a Ka-band Nadir Radar Altimeter: First Results and Impact on Future Altimetry Missions

Bruno Picard [1], Nicolas Picot [2], Gérald Dibarboure [2] and Nathalie Steunou [2]

[1] Fluctus SAS, 81800 Rabastens, France; bpicard@satobsfluctus.eu
[2] CNES, 31400 Toulouse, France; nicolas.picot@cnes.fr
[2] CNES, 31400 Toulouse, France; gerald.dibarboure@cnes.fr
[2] CNES, 31400 Toulouse, France; nathalie.steunou@cnes.fr
* Correspondence: bpicard@satobsfluctus.eu; Tel.: +33-6659-322-67

Abstract: The impact of large atmospheric attenuation events on data quality and availability is a critical aspect for future altimetry missions based on Ka-band altimetry. The SARAL/AltiKa mission and its Ka-band nadir altimeter offer a unique opportunity to assess this impact. Previous publications (Tournadre et al. 2009, 2015) already analyzed the impact of rain on the waveforms at Ka-band and proposed a definition of an elaborate rain flag. This notion tends to give a simpler black and white view of the atmospheric attenuation when the effect on the altimeter measurement is intense. But in practice, there is continuum of measurements that may be partially distorted or corrupted by rain events. The present study proposes a wider point of view , the ACECAL approach providing statistics on rain cells occurrences as well as their amplitude and their size, as guidelines for future Ka-band missions concerning the impact of the atmosphere. At global scale, 1 % of the measurements are affected by an attenuation larger than 23 dB and 10 % of the atmospheric attenuation events have a size larger than 40 km. This study demonstrates that the data quality and availability over some regions of particular interest for oceanography as Gulf Stream, North Pacific and Brazil currents could be affected compared to global statistics. It also opens some perspectives on the benefits that the community could be drawn from the systematic distribution of the rain cells parameters as secondary products of altimetry missions.

Keywords: rain cells; atmospheric attenuation; microwave radar; Ka-band; altimetry;

1. Precipitation and atmospheric attenuation in the context of altimetry missions

Satellite altimetry missions measure the sea surface height (SSH) at a global scale and an increasing accuracy since 1992 [1]. The altimeter signal is traditionally emitted in the Ku-band at around 13.5 GHz as used by Topex (13.6 GHz) and Poseidon (13.65 GHz) altimeters [2] up to the latest Jason-3 (13.6 GHz) and Sentinel-3 (13.575 GHz) series [3].

The attenuation of microwave radar pulse depends on the moist air refractivity index, characterized by the pressure, the temperature, the water vapor, the cloud liquid water content and the rain rate. When the attenuation is too large, the shape of the waveform measured by a classical nadir altimeter is too far from the theoretical Brown model and the retracking algorithm fails to estimate the geophysical parameters: the range, the surface wave height (SWH), the backscattering coefficient (σ_0) from which the wind speed is computed, and the slope of the trailing edge related to the altimeter mispointing angle. But even with lower distortions, the error on these parameters could be unacceptable with respect to the budget error.

Atmospheric attenuation ($\Delta\sigma_0$) at Ku-band has been specifically characterized since the very beginning of the spatial altimetry era. Ku-band being mostly affected by rain, early papers [4,5] are dedicated to characterized the impact of rain on the Topex/Poseidon observations. Rain flag and even rain rate are estimated from the difference between altimeter backscattering coefficients at the main Ku-band and the secondary C-band. Later on, the parameterization of the Ku/C σ_0 relation is updated for Jason-1 and the Ku/S σ_0 relation for Envisat [6,7]. Validation against Tropical Rainfall Measuring Mission (TRMM) observations shown better performances using the

Preprints (www.preprints.org) | NOT PEER-REVIEWED | Posted: 28 September 2021 doi:10.20944/preprints202109.0477.v1

Tournadre relation [8]. The different studies agree on a proportion of measurements affected by rain of between 1% and 5% of the total number of observations of ocean.

The CNES/ISRO SARAL/AltiKa mission launched in 2013 was the first attempt for an altimetry mission to use a central frequency in the Ka-band at 35.75 GHz. Using a higher frequency allowed to reduce the footprint of the altimeter from 15 km at Ku-band to 4 km, but also the range noise and the impact of the ionosphere [9]. The major counterpart in terms of SSH monitoring is a larger sensitivity to the water in the atmosphere: the altimeter backscattering coefficient atmospheric attenuation is 7 times larger at Ka-band than at Ku-band [10]. Before the launch of SARAL/AltiKa mission, the expected impact of rain onto altimeter waveform and the foreseen percentage of non-valid data have been studied, and a, innovative algorithm to flag the data has been developed in two successive papers by Tournadre et al. [11,12]. The authors analyzed the effect of cells onto altimeter measurement using empirical relation for attenuation and simulated waveforms. The amplitude of the rain events but also the variability over the altimeter footprint size both have an impact. The validation performed over actual measurements [13] shown the good performance of the so-called Matching Pursuit (MP) flagging algorithm and a better availability of the observations than expected in the pre-flight study [11] due to a particularly good signal-to-noise ratio of the radar altimeter.

The role of the precipitation systems in climate models and the need for a better understanding of their geometrical and physical properties is well introduced by [14]: the framework is complex, especially the characterization of the rain cell size distribution as it is discussed in [15]. Even the definition of a rain cell is subject to discussion. Within the current study, we will use the term "cell" for a rain field (also called rain area) that may be composed by one or several peaks of large attenuation, as illustrated by the Figure 2 in the same paper. The authors also found that most of single-peaked areas have a diameter smaller than 15 km. Illustrations of different type of rain cells are shown here in the Figure 2 and the Figure 3.

The cell size distribution is mainly investigated using on ground-based radar in particular locations [15–18]. The use of dedicated satellite missions and instruments such as the precipitation radar (PR) and the Microwave Imager (TMI) on-board TRMM increases the geographical coverage, with new challenges to address, as how to fit the shape of the cells or how the swath truncation affects the results [14,19,20]. [21] already demonstrated that Ku-band altimetry missions provide useful information on the distribution of cell size that confirmed the results of the literature but also increase the global coverage to higher latitudes than covered by TRMM.

In the continuity of this work and considering the results for the Ka-band presented in [13], the present paper aims at characterizing the short-scale atmospheric attenuation variation within rain cells detected by the MP flag, both in terms of amplitude and size. One objective is to assess the impact of the atmospheric attenuation on the data availability thant remains critical for the future interferometric missions based on Ka-band measurements such the CNES/NASA Surface Water and Ocean Topography (SWOT) mission to be launched in 2022. Another one is to illustrate how Ka-band altimetry is particularly well-fitted to characterize rain cells, in complement to dedicated tropical missions.

Based on the analysis of SARAL/AltiKa altimeter backscattering coefficient, the first part of this paper is dedicated to the definition of a simple detection algorithm of attenuation cells defined as short-scale drops of the attenuation related to the impact of rain cells. In a second part, the amplitude and the size of those cells are characterized and discussed in terms of occurrences and geographical distribution. Finally, a discussion is conducted in the conclusion on the potential impact on oceanography applications.

2. Detection and characterization of rain cells

2.1. Ka-band atmospheric attenuation

The atmospheric attenuation (hereafter reffered as $\Delta\sigma_0$) is the sum of a dry component $\Delta\sigma_0^{dry}$ depending on pressure (p) and temperature (t), a wet component $\Delta\sigma_0^{wet}$ proportional to the total column water vapour content (TCWV), a liquid component ($\Delta\sigma_0^{liq}$) depending on the liquid water path (LWP) and a component $\Delta\sigma_0^{rain}$ proportional to the rain rate (RR).

Preprints (www.preprints.org) | NOT PEER-REVIEWED | Posted: 28 September 2021 doi:10.20944/preprints202109.0477.v1

[10] proposed a polynomial empirical relation of some atmospheric components to compute Ka-band and Ku-band attenuations from ECMWF analysis. However, this approach is limited for the study of short temporal and/or spatial scale attenuation events since (1) it requires an interpolation between two successive analysis separated by 6 hours, (2) the location of clouds and their associated liquid water content is not accurate as for any Numerical Weather Prediction (NWP) model and (3) the rain rate is not part of the analysis dataset when it is critical for Ka-band.

The microwave radiometer (MWR) on-board the SARAL/AltiKa mission has a better spatial resolution (about 12 km) and provides retrieval of atmosphere-related retrievals simultaneously to the altimeter observations. The wet tropospheric correction retrieved from the brightness temperatures (TB) shows very good performance as demonstrated in [22]. Nevertheless, due to the coarser spatial resolution and sampling compared to the altimeter, the radiometer $\Delta\sigma_0$ underestimates the amplitude of the attenuation over rain cells. As illustrated by the Figure 1, the geographical distribution of the atmospheric attenuation retrieved by the radiometer is mainly driven by the distribution of the water vapor with values less than 2 dB. The Figure 2 also shows how strong attenuation of the σ_0 (blue dots) are largely underestimated by the radiometer (brown solid line).

The originality of the current approach is to take benefit from a direct measurement of the variation of the Ka-band altimeter backscattering coefficient, with a fine spatial resolution (about 4 km, slightly better than the PR on-board TRMM) combined to a very fine temporal sampling (40 Hz). As illustrated by Figure 2, the along-track σ_0 timeseries contain a fine spatial description of attenuation cells with a corresponding spatial sampling of about 175 m. The SARAL/AltiKa mission thus offers a unique opportunity to study the small-scale variation of the Ka-band $\Delta\sigma_0$.

Tournadre (2006) already estimates the characteristics of rain cells from Jason-1 and Envisat Ku-band rain attenuation $\Delta\sigma_{0\mathrm{Ku}}$, basically obtained from the difference between the 1 Hz Ku-band and C- or S- band σ_0: any measurements where $\Delta\sigma_{0\mathrm{Ku}}$ is larger than 0.5 dB when LWP is larger than 200µm is considered under rainy conditions. The rain cell chord distribution (RCCD) is established from the number of consecutive measurements under rainy situations. Indeed, altimeters do not measure directly the diameter of the rain cell but its chord, since the altimeter track randomly sample the two-dimensional rain cells. [17] established a relation between the RCCD and the rain cell diameter distribution (RCDD). The mean chord of the RCCD and the mean diameter of the RCDD are proportional with a factor of $\frac{2}{\pi}$, assuming circular-shaped rain cells. This relation is useful to translate one-dimensional information as provided by SARAL/AltiKa to two-dimensional cases that will be encountered by the future SWOT mission, even if the actual shape of rain cells is more likely to be elliptical over ocean [20] or even without any particular shape [14]. The statistics of rain rates and cells sizes provided by [21] are mostly confirmed by the existing literature, but the Figure 2 shows the limits of this approach, being (1) the spatial resolution of the Topex and Jason-1 altimeter were coarser than for AltiKa (2) the study was based on 1 Hz measurements (separated by 6 km) (3) the Ku-band is seven times less sensitive to rain than Ka-band.

The following section describes the new algorithm used to characterize attenuation cells directly from Ka-band SARAL/AltiKa altimeter from 40 Hz σ_0 timeseries.

2.2. Description of the datasets

This study makes use of the dataset provided by the Prototype for Expertise on AltiKa for Coastal, Hydrology and Ice (PEACHI) initiated to deliver of a long series of research-grade Level-2 product notably featuring innovative retracking algorithm [23]. All the parameters defined below are included in this dataset which is available at the high data rate of 40 Hz and at the compressed data rate of 1 Hz.

The period of interest covers the whole year 2015, from AltiKa cycle 20 (starts on the 8th of January 2015) to cycle 30 (ends on the 28th January 2016). It corresponds to the strong 2014-2016 El Niño event. At global scale, the precipitation over ocean is larger than the long-term average, in keeping with the five previous years. The increase of rainfall was particularly high in the Pacific Ocean over the Inter-Tropical Convergence Zone (ITCZ), western and eastern Pacific Ocean and over Indian Ocean. On the contrary, a strong negative rainfall anomaly was observed

Preprints (www.preprints.org) | NOT PEER-REVIEWED | Posted: 28 September 2021 doi:10.20944/preprints202109.0477.v1

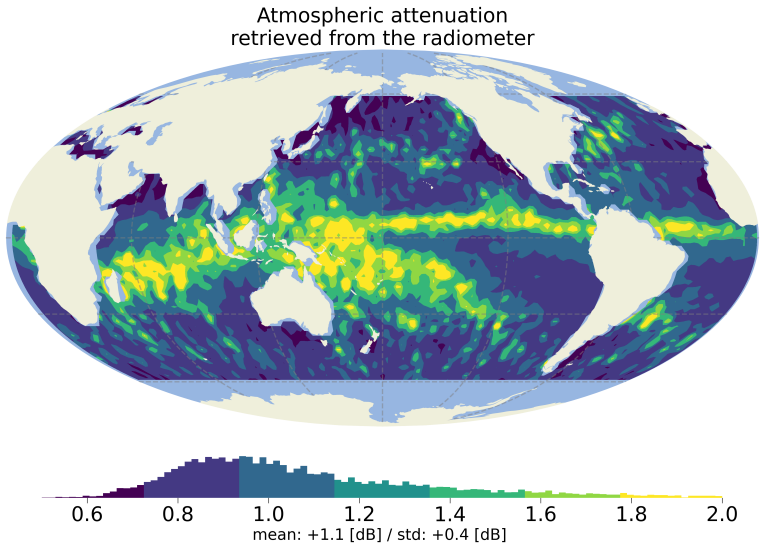

Figure 1. Geographical distribution of the atmospheric attenuation retrieved by the radiometer on-board SARAL/AltiKa mission (bin average over a 2°x2° grid, cycle 20 to 30).

over the seas of the Maritime Continent and a below-normal precipitation occurred in the northern and southern Pacific Oceans [24]. The question of the representativity of this particular year with respect to an average situation is difficult to answer considering the high inter-annual and spatial variability of the precipitation. Still, the results presented here should provide useful information for the future missions.

A specificity of our approach is to base our analysis on the σ_0 timeseries estimated from the adaptive retracking applied on 40 Hz waveforms. This new solution is relying on the Nelder-Mead method implemented with an exact likelihood criteria for low resolution mode measurements [25]. The main benefit for the current study is the capability of this retracking to provide a σ_0 less correlated to the other parameters retrieved from the waveform (range and significant wave height): the backscattering coefficient statistics are more representative of atmosphere and surface conditions.

2.3. Definition of the ACECAL algorithm

The Figure 2 shows a typical rain cell selected according to the criteria detailed in the following paragraph. On the abscissa is reported the distance from the first measurement. The blue dots show the 40 Hz σ_0 timeseries retrieved from the adaptive retracking. The segments are selected based on the MP rain flag that is raised along about 40 km (see the orange dotted line). The variation of the σ_0 can generally be explained either by surface or by atmospheric conditions. Since both shares a common range of spatial scales and amplitude of their impact on the backscattered signal, it is difficult to discriminate between the two, for instance to distinguish between the scattering due to large surface wave height and the attenuation due to rain [REF]. Large-scale variation of the atmospheric attenuation is usually well captured by the retrieval from the radiometer observations. But the combination between an empirical approach for the estimation and the coarse spatial resolution of MWR observations (see the 37 GHz Tb values in solid violet lines) leads to a clear underestimation of the atmospheric attenuation under rainy conditions (brown solid line). Those events represent less than 10% of the global atmospheric conditions and the neural network used for the operational processing under-performs for events so under-populated in the learning database.

Indeed, on top of the large-scale variation, the internal structure of the rain cell is seen through the Gaussian-shaped peaks with an attenuation of about 5 dB with respect to the background. The 37 GHz Tb value of more than 220 K clearly identifies this pattern as the result of atmospheric conditions but the retrieved atmospheric attenuation is only of about 4 dB, only 2 dB above the estimated background. These situations are typical of a one-dimensional cut of a two-dimensional precipitation field. As highlighted by [26] when he defines a rain cell model

Preprints (www.preprints.org) | NOT PEER-REVIEWED | Posted: 28 September 2021 doi:10.20944/preprints202109.0477.v1

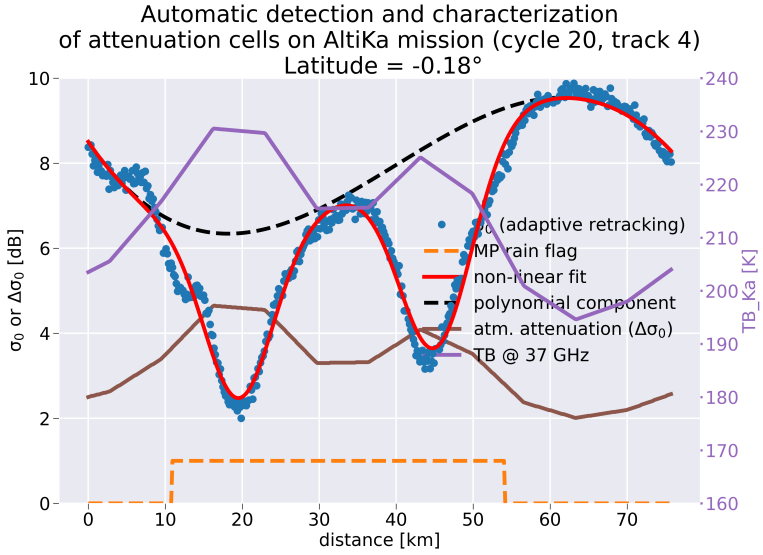

Figure 2. Illustration of the Attenuation Cells Caracterization Algorithm (ACECAL) algorithm applied on two segments extracted from the pass 4 of SARAL/AltiKa cycle 20 (January 2015)

to assess its impact on altimeter waveform, a Gaussian shape for the rain-rate falloff, even if idealized, is well adapted for rain rates up to 50 mm.h^{-1} [16].

Setting out from this premise, the core of the Attenuation CElls Characterization ALgorithm (ACECAL) relies on a non-linear least-square fit of the σ_0 timeseries, where the fitting model uses a combination of a 3-degree polynomial and a pre-defined number of Gaussians. The implementation of this approach is performed using the LMFIT python library [27]. This algorithm provides an estimate of the location, the chord and the amplitude of the rain cells that impact the Ka-band σ_0. The following paragraphs describe the pre-processing applied before the selection of segments where rain conditions occur, the processing that leads to the characterization of the attenuation cells and its limitations.

2.3.1. Pre-processing

Several editing criteria are applied to the measurements to select segments identified as under rain events conditions, before running ACECAL. The parameters in italic refers to the name of the fields in the PEACHI products available in NetCDF format. The selection criteria are summarized in Table 1.

In order to select open ocean conditions only, the following values or thresholds are used. The measurement should lye over ocean (`surface_type == 0`), not over identified sea ice (`ice_flag == 0 and abs(latitude) <= 60°`) and at a distance larger than 50 km from the coast (`distance_shoreline > 50 km`). This latter criterium ensures that the brightness temperatures observed by the MWR are not impacted by the coast, which leads to an increase of the value that could be falsely interpreted as an increase of the precipitations. The value of σ_0 and the robustness of the rain flag are also impacted by orbit maneuvers leading to mis-pointing periods: the off-nadir angle of the platform should be null (`off_nadir_angle_pf == 0`).

The MP rain flag is used to select the segments where rain conditions occur. To increase the robustness of the polynomial fit, a margin of 10 km or 15% of the segment size is added on both sides, respectively for a size of less or more than 100 km.

Finally, the σ_0 timeseries should obviously not be corrected from the atmospheric attenuation. Since it is the case in PEACHI products, the atmospheric attenuation (`atmos_corr_sig0_40hz`) is systematically subtracted to the corrected σ_0 (`sig0_adaptive_40hz`) before the analysis.

2.3.2. Processing

As pointed out by Tournadre et al. 2015, the MP flag is also sensitive to bloom events, where the ocean surface is smooth, resulting in large σ_0 values and short scale variation of the

Preprints (www.preprints.org) | NOT PEER-REVIEWED | Posted: 28 September 2021 doi:10.20944/preprints202109.0477.v1

Table 1: Criteria for the selection of segments impacted by rain and the selection of attenuation cells within those segments.

Pre-processing		
Parameter	**Criteria**	**Comment**
`surface_type`	== 0	open ocean
`ice_flag`	== 0	no sea ice
`distance_shoreline`	$\geq$ 50 km	no land contamination on TB
`off_nadir_angle_pf`	== 0	no platform maneuvers or depointing
Post-processing		
Parameter	**Criteria**	**Comment**
`trailing_edge_variation_flag_40hz`	== 1	MP flag raised (potential rain event)
`sig0_adaptive_40hz - atmos_corr_sig0_40hz`	<15 db	no bloom
short-scales / large-scales windows size	1.5 km / 30 km	to select attenuation cells
minimum amplitude of the attenuation due to rain cells	$\geq$ 0.5 dB	to ensure the robustness of the fit
value of 37 GHz TB at the maximum attenuation	$\geq$ 175 K	to ensure the detection of rain event

off-nadir angle. The authors rely on the radiometer LWP to discriminate between actual rain events and surface blooms: any measurements flagged by the MP approach with LWP below 0.1 kg/m^2 are classified as bloom events. But it happens that high values of σ_0, representative of bloom conditions, are associated to high values of 37 GHz TB, this latter being directly related to the radiometer LPW. It is thus chosen here to apply a maximum threshold of 15 dB directly to σ_0: if it exceeds this limit within the selected segment, the segment is discarded. The value of the threshold is arbitrary but has a weak impact on the eventual robustness of the results thanks to the sequencing of filtering steps presenting below.

If the segment is selected, the first step consists on determining the number of peaks and the index of their maximum. The peaks are isolated from a residue obtained by the difference between a short-scales and a large-scales median filter applied to the original σ_0 timeseries. The small-scales filter has a window size of about 1.5 km (10 successive measurements), removing the small-scales noise and allowing a better location the peak maxima. The large-scale filter has a window size of 30 km, removing the large-scale variations of the signal. The size of this windows has been chosen in agreement with the global distribution of the rain cell size as established in the literature. Goldhirsh (1983) [28] shows that less than 10% of the cells corresponding to light rain rate events (2 mm.h^{-1}) have a size larger than 30 km, less than 4% for rain rates of 5 mm.h^{-1}. For Begum et al. (2009) [18], it is even less than 1% for the same rain rate. For larger rain rates, the maximum size is below 15 km. The sub-segments containing peaks are isolated from the sections where the residue is larger than 0.5 dB. If this criterion is not fulfilled, the segments is discarded. This limit of 0.5 dB has been selected to reinforce to distinction between surface and atmospheric impact on the σ_0. As pointed out in the following section, this limit could be relaxed in future version of the ACECAL approach. Over each selected section, the position of the maximum is found.

To select rainy conditions amongst the different conditions where the MP flag is raised, we choose here to apply a threshold on the 37 GHz TB rather than on the LWP. The retrieval algorithm for the LWP is depending on the σ_0 and as said above, with values potentially out of the optimal range of validity of the neural network under rainy conditions. A threshold on the 37 GHz TB, being more sensitive to LWP than the 23.8 GHz channel, is more straightforward

Preprints (www.preprints.org) | NOT PEER-REVIEWED | Posted: 28 September 2021 doi:10.20944/preprints202109.0477.v1

and independent from any retrieval algorithm, including the retracking algorithm used to estimate the σ_0. Only the sections where the maximum of the cell corresponds to a value of the 37 GHz TB larger than 175 K are eventually selected ($tb\_ka > 175$ K). This value has been established empirically based on the monitoring of both the 37 GHz Tb and the surface wave height and offers the best robustness, even if some actual cells may be not selected.

The non-linear model is defined as the combination of a 3-degrees polynomial and a number of Gaussians equal to the number of selected peaks. The initial positions of the Gaussians are used as initial values. The fit being weakly dependent on the values of the amplitude and the sigma of the Gaussian, their values are fixed to respectively to -250 and 2, as recommended by the LMFit library. The fit is then applied to the non-filtered σ_0 timeseries inside the whole segment.

The Figure 2 shows the result of the fit as the red solid lines, the dashed black lines referring to the polynomial components. On these examples, the fit succeeds to reproduce the variation of the background and the shape of the individual peaks. The figure also illustrates how the ACECAL approach provides a finer description of the situation within the rainy area than the MP flag: the actual number of observations within the attenuation cell may be larger than the observations flagged by the MP approach and the inner structure is clearly not uniform. The location of the maximum and the width of the peaks are well estimated, with small uncertainties (respectively less than 0.5 dB and less than 2 km).

The location of the minimum and the value of the minimum are computed for each Gaussian detected within a segment. The full width at half maximum (FWHM $\approx 2.35482\sigma$) and the six-σ full width (FW6S = 6σ) are deduced from the standard deviation of the Gaussian σ.

The size of the rain cell is defined by distance covered by the sum of the FW6S of each individual peak, accounting for overlapping if it occurs. In the cases illustrated by the middle and the bottom panel of Figure 3, this size is close to the size where the MP flag is raised. In the case illustrated by the top panel, the size of the cell is computed as the sum of the width each individual peak. Under this particular condition, those peaks should have been considered individually since they are clearly individual cells. This is a current limitation of ACECAL that does not include a criterion on the separability of the peaks.

The maximum of the attenuation within a peak is defined as the difference between the minimum value of σ_0 and the polynomial fit at the same location. Rather than focusing only on the absolute value of the σ_0 at the maximum, this definition for the attenuation is consistent of the objective of the study being the impact of rain cells onto the backscattering coefficient. In the case of the retrieval of a 2D-field as with the SWOT mission, the distribution of rain cells will appear as elliptical-shaped areas with stronger attenuation over a background at a given amplitude. In the perspective of validation activities, it is more valuable to characterize the difference between the background and those areas.

During the year 2020, 56000 rain cells are detected by the ACECAL method and, within these rain cells, 84500 peaks are identified.

2.3.3. Illustrative cases and zonal distribution of occurrences

The Figure 3 illustrates how the method succeeds to fit complex conditions and provides a finer level of information than given by the MP flag. The top panel shows a long segment of 400 km, where is MP flagged is raised but the ACECAL approach detects only a limited distant cell, the last one lying in an area where the MP flag is actually not raised. Even when the situation is complexified by the presence of large rain rates (associated with 37 GHz TB values larger than 230 K), the ACECAL approach provides a fit very close to the σ_0 timeseries (see the middle and bottom panels). Nevertheless, the polynomial may not be optimal, and the resulting attenuation may be overestimated, as shown by the bottom panel.

The percentage of 40 Hz observations flagged respectively by the MP approach and the ACECAL method with respect to the total number of 40 Hz observations over open ocean (defined by the criteria of the pre-processing, see Table 1) are of the same order. The zonal variation for the MP flag is close to the results presented in the Figure 5 in Tournadre et al. 2015: a maximum of 10%s over the ITCZ, with two secondary maxima at 5% around 40°N and 40°S along the mid-latitude storm tracks. Only the dissymmetry between Northern and Southern hemisphere in

Preprints (www.preprints.org) | NOT PEER-REVIEWED | Posted: 28 September 2021 doi:10.20944/preprints202109.0477.v1

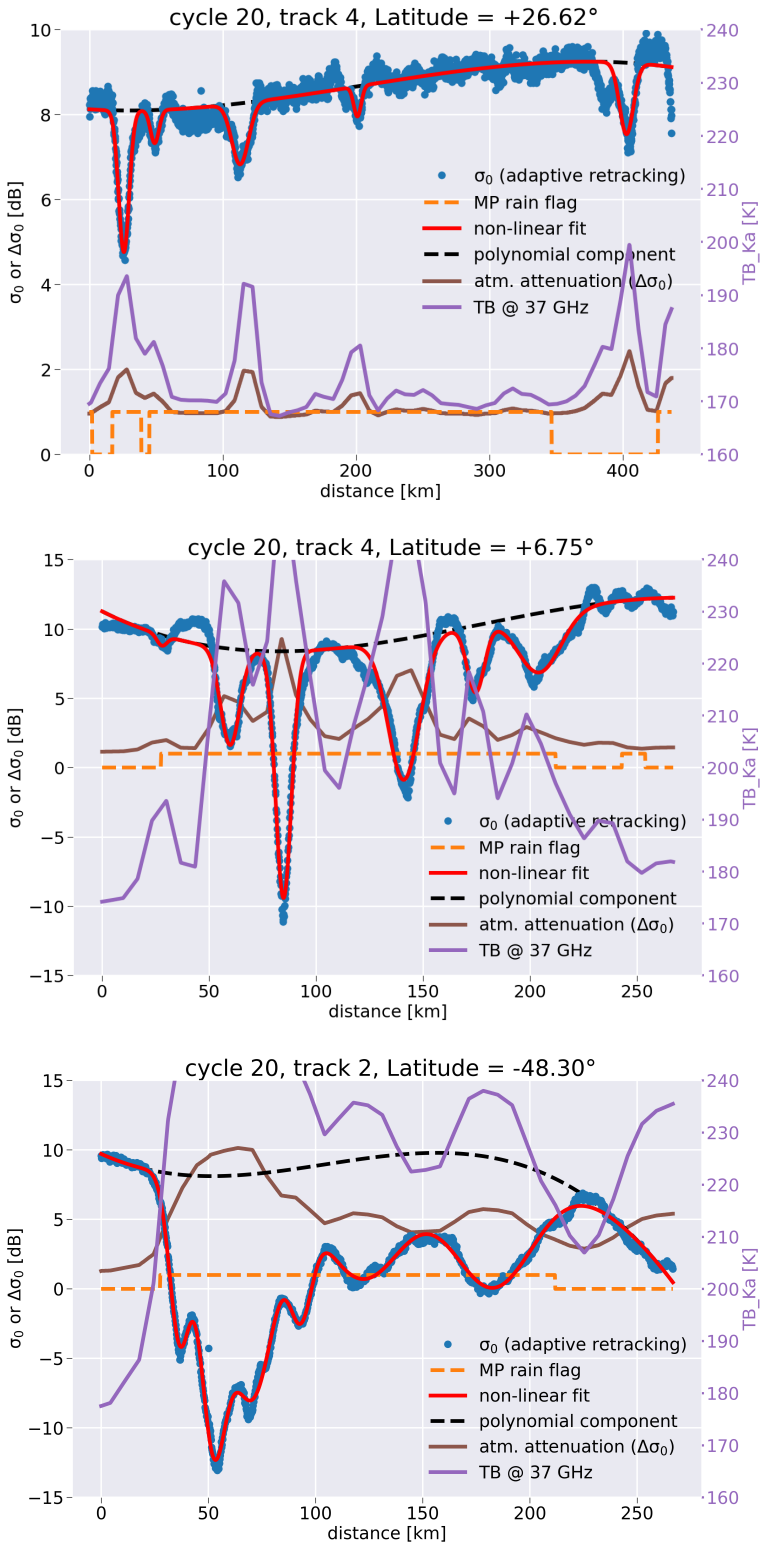

Figure 3. Examples of complex situations with multiple peaks detected by the ACECAL approach. Top: a long segment of 400 km, where is MP flagged is raised but the ACECAL approach detects only a limited number of individual cells, the last one lying in an area where the MP flag is actually not raised. Middle: even when the situation is complex, the ACECAL succeeds in detecting five different peaks. Bottom: the impact of the atmosphere is strong and probably associated to a large rain rate (large values of TB). The ACECAL approach detects six peaks but the polynomial fit is probably not optimal.

Preprints (www.preprints.org) | NOT PEER-REVIEWED | Posted: 28 September 2021 doi:10.20944/preprints202109.0477.v1

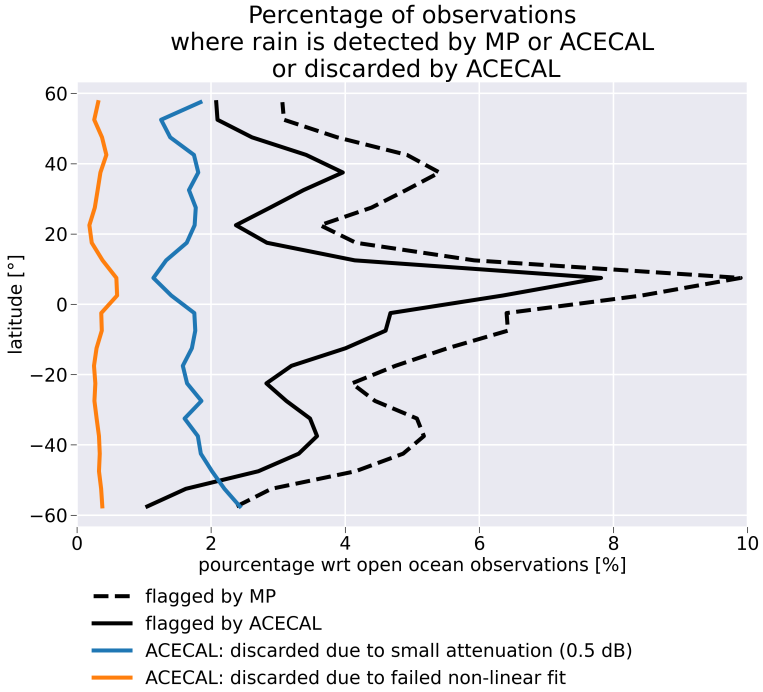

Figure 4. Variation with the latitude of the percentage of 40 Hz data where rain is detected by the MP approach (dotted black line) or the ACECAL approach (solid black line) and percentage of data discarded by the ACECAL approach due to attenuation below the minimum threshold (0.5 dB) (solid blue line) or because de non-linear fit failed (solid orange line).

terms of climatological distribution of the precipitation in not seen here but may be due to some particularity of the year 2015.

The percentage of observations detected by ACECAL is smaller by about 1%. As said above, the percentage of observations where the non-linear fit failed to converge is small, lower than 0.5%, with no particular zonal distribution. The percentage of observations initially flagged by the MP approach but not selected in input to ACECAL is close to 2% with a small zonal distribution as well. This smaller percentage is explained by the fact that the ACECAL processing is relying on the MP flag but apply a stringent criterium on the minimum attenuation for a cell to be detected. But there may be some compensation effects between peaks detected outside the area (larger number of flagged observations) and narrow peaks within the area (smaller number of flagged observations). The distinction between these two situations is not investigated further within the frame of the current study. Amongst the leads for further improvement of the ACECAL approach, it could be interesting to propose a solution that is not dependent on the MP flag and to assess if the lower threshold of 0.5 dB on the attenuation could be overcome.

3. Amplitude and size of attenuation cells retrieved from SARAL/AltiKa mission

3.1. Amplitude of attenuation cells

The Table 2 summarizes the results discussed hereafter. The Figure 5 shows different metrics that characterize the relative attenuation (with respect to the fitted background) at the maximum of the peaks detected with ACECAL, thus corresponding to a worst-case scenario.

The geographical distribution of the attenuation is consistent with the strongly zonal distribution of water vapour and precipitation (Figure 5, top panel). The amplitude is four times larger than the attenuation computed from the radiometer (see Figure 1) or using NWP analysis (Figure 2 in Lillibridge 2014); it better reflects the actual impact of the rain onto the backscattering coefficient and consequently illustrates the benefits of the ACECAL approach. As expected, over dry regions where upwelling occurs, no cells are detected or with attenuation of the order of 1 dB. On the opposite, the maximum attenuation is larger than 8 dB along the ITCZ but also over the

Preprints (www.preprints.org) | NOT PEER-REVIEWED | Posted: 28 September 2021 doi:10.20944/preprints202109.0477.v1

regions impacted by the India monsoon. Other regions of particular interest for the altimetry are also impacted. For instance, over the Brazil current, over the South Atlantic Convergence Zone, the attenuation shows values larger than 8 dB.

The zonal distribution of the amplitude (Figure 5, middle panel) shows that the averaged amplitude varies from 2 dB at high latitudes to about 7 dB at ITCZ, but considering the average plus the standard deviation, the amplitude is about 6 dB for latitudes below 40° and can reach 14 dB in the ITCZ.

The bottom panel of the Figure 5 displays the percentiles of the absolute value of σ_0 at the maximum of the peaks (see the dotted black lines): for 10% of the strongest attenuation peaks, the $sigma_0$ can reach values lower than -7 dB, to be compared to a value of +10 dB under clear-sky conditions. Now focusing on the relative attenuation (see the solid black line), the median at the maximum of the attenuation peaks is about 3.5 dB and 10% of the peaks have a maximum attenuation of 13 dB. As illustrated by the middle panel, the attenuation strongly depends on the latitudes and the orange and blue solid lines respectively show the attenuation at high latitude (above 45°) and below 10°: the 10^{th} percentile is larger than 15 dB over the equatorial region.

The statistics on the attenuation can be roughly translated to hourly rain rates in order to validate the results. The Marshall-Palmer parameterization of [29] is used for a frequency of 35.75 GHz. Assuming a thickness of 6 km for the rain layer, the median attenuation for the peaks of 3.5 dB corresponds to a rain rate of about 1.2 mm.h^{-1} and the 1^{st} percentile of 23 dB to a rain rate of about 8 mm.h^{-1}. The Table 2 also contains the results assuming a 3 km thickness: [14] uses PR measurements with a similar spatial resolution and exhibit a double peak of the thickness distribution over ocean at 3 km for shallow isolated precipitation and 6 km for deep rain cells. Those results for SARAL/AltiKa are in agreement with [14] who reported an average rain rate over ocean varying between 0.4 mm.h^{-1} and 8 mm.h^{-1} with a peak at 1 mm.h^{-1}, even if the two datasets cannot be directly compared: [14] provides results limited to the Tropics and averaging all rain conditions when the results presented here in the Table 2 are extended up to high latitudes but concerns the maximum attenuation within the peaks. The statistics are also in good agreement with the results established from Ku-band altimetry missions by [21] where the rain rate varies between 1.5 mm.h^{-1} and 10 mm.h^{-1} with a peak around 2 mm.h^{-1}.

3.2. Diameter of rain cells

The estimation of the rain cell chord length provided by ACECAL is translated to the equivalent circular-shaped diameter using the relation established by [17]. The top panel of Figure 6 displays the geographical distribution of this diameter. The larger cells are detected at high latitudes associated with smaller the attenuation. As shown by the zonal distribution of the size (Figure 6, middle) and as highlighted by Nesbitt et al. (2006), a minimum is observed around $\pm 20°$ latitude, above the semipermanent highs associated to clear sky conditions. Nevertheless, the contrast between tropical regions and high latitudes is small in average: the mean diameter is about 20 km below the Tropics against less than 25 km for latitudes around 40°, along the storm track. Considering now the average plus the standard deviation, the contrast is slightly larger, with larger variability at higher latitudes and a diameter larger than 45 km. The bottom panel of Figure 6 displays the percentile of the rain cells diameter (solid lines). On the contrary to the previous metrics, the distribution of the diameter shown here is not impacted by any averaging. The median of the diameters is equal to 15 km and rain cells with diameters larger than 40 km represent about 10% of the population. The difference between the percentiles of the diameters for rain cells lying around the Tropics (solid blue line) or at higher latitudes (orange solid line) is small.

The ACECAL approach also provides information on the diameter of the internal peaks. We chose to display the metrics for the FWHM of the peaks, which is more consistent with the maximum attenuation shown in Figure 5. At a global scale, the geographical distribution is smooth: the diameters of the peaks are larger than 6 km along the Tropics or at latitudes larger than 40°, with a minimum below 5 km along the semipermanent highs. As seen in the bottom panel of Figure 6 by the dotted lines, the median of the peak diameter is 5 km and 10% of the peaks have a diameter larger than 10 km.

Preprints (www.preprints.org) | NOT PEER-REVIEWED | Posted: 28 September 2021 doi:10.20944/preprints202109.0477.v1

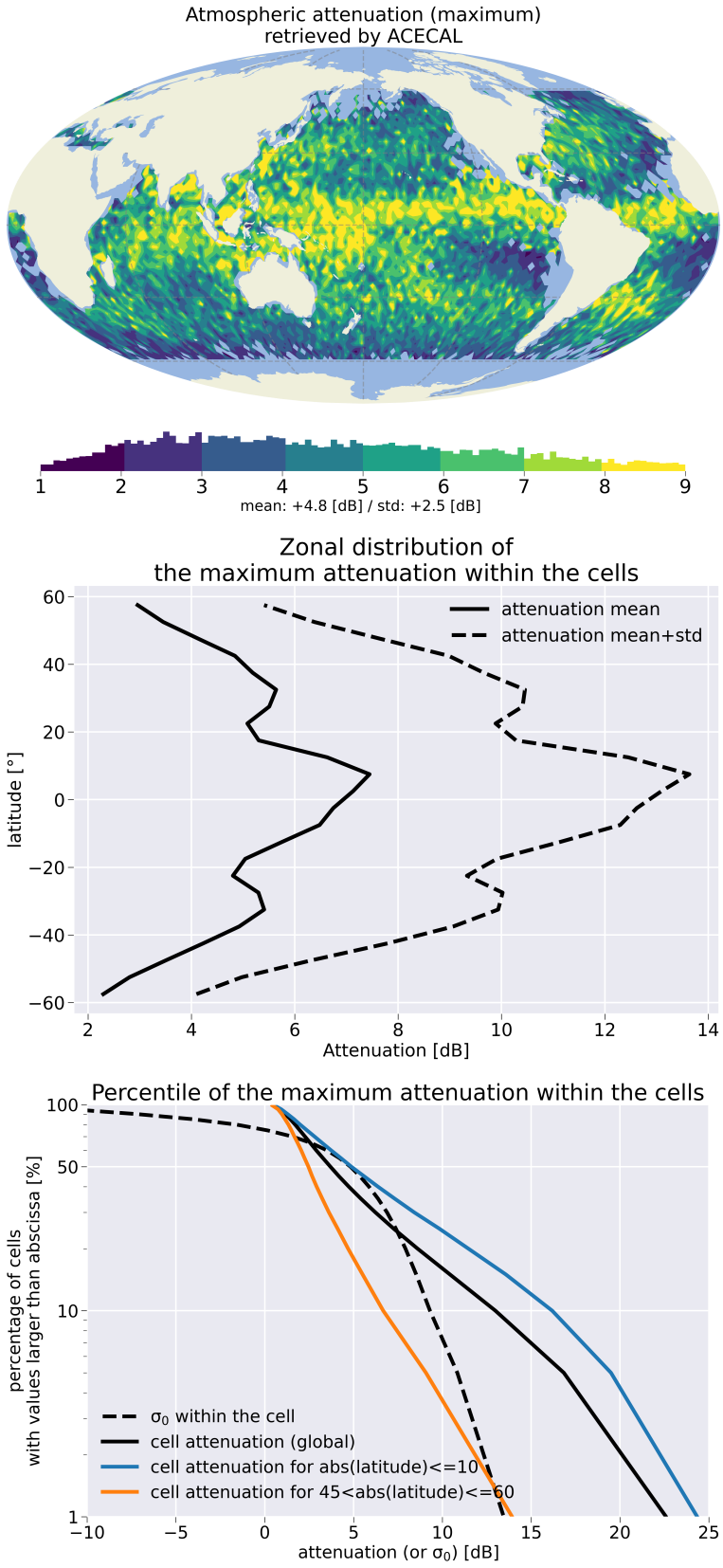

Figure 5. Characteristic of the amplitude of atmospheric attenuation cells at Ka-band. Top: geographical distribution and associated histogram. Middle: zonal distribution of the averaged amplitude (solid line) and the average plus the standard deviation (dotted line). Bottom: the percentile of the absolute value of σ_0 and of the attenuation (SARAL/AltiKa cycles 20 to 30, year 2015)

Preprints (www.preprints.org) | NOT PEER-REVIEWED | Posted: 28 September 2021 doi:10.20944/preprints202109.0477.v1

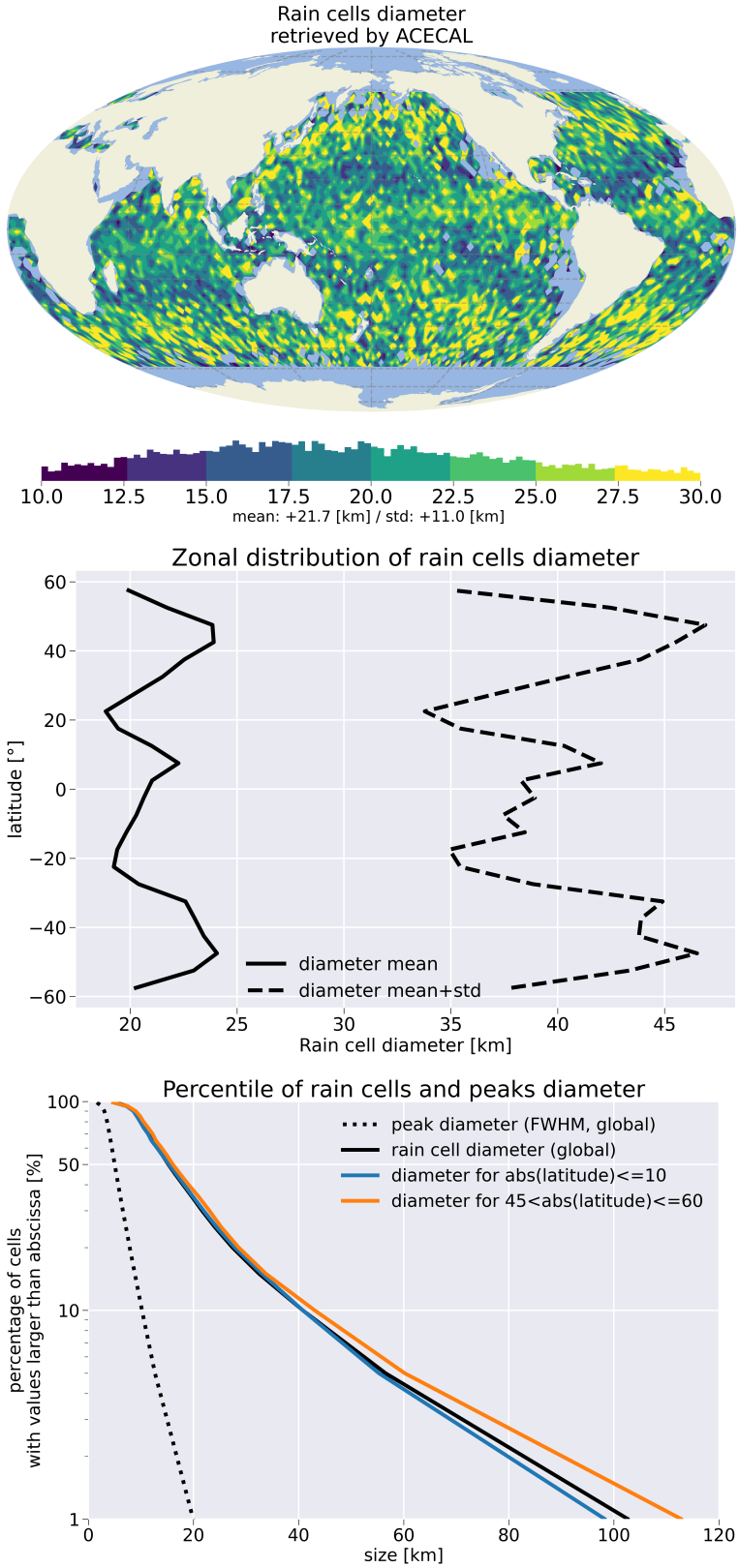

Figure 6. Characteristic of the atmospheric attenuation cell size at Ka-band. Top left, geographical distribution and associated histogram. Top right, zonal distribution of the averaged size (solid red line) and the average plus the standard deviation (solid green line). Bottom, the percentile at global scale and for zonal selections. (SARAL/AltiKa cycles 20 to 30, year 2015)

Preprints (www.preprints.org) | NOT PEER-REVIEWED | Posted: 28 September 2021 doi:10.20944/preprints202109.0477.v1

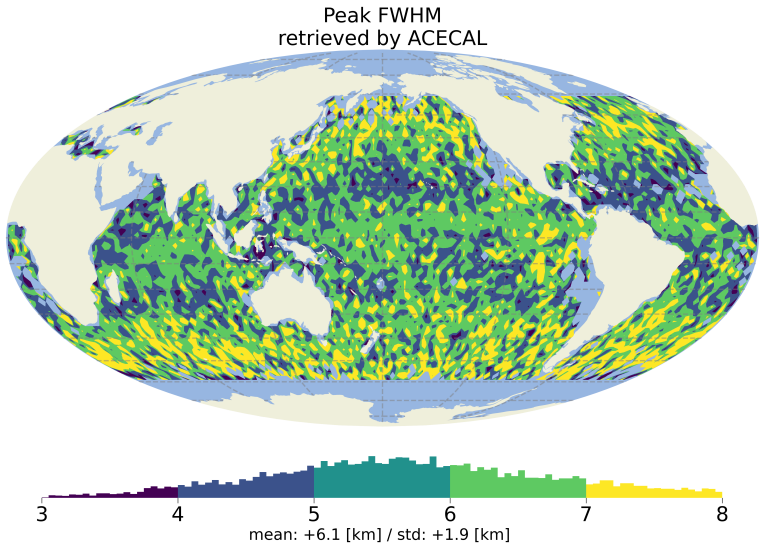

Figure 7. Geographical distribution of peaks diameter (FWHM) within the rain cells (bin average over a 2°x2° grid, cycle 20 to 30).

Those results are also in agreement with previous studies. [14] computes a median length and width of respectively 20 km and 15 km over ocean over the region covered by TRMM, close to the median found in the present study. [19] discussed more into details the geographical distribution of the size of rain cells (see their Figure 8). The feature's maximum dimension (FMD) is computed as twice the major axis of the ellipse that fits the rain cell: the maximum of the FMD is located over the ITCZ and in the subtropics. Over ocean, it varies between 10 km and 20 km, with a minimum of about 7 km over the dry upwelling regions. Those results are slightly more contrasted than the distribution shows in Figure 6 but both the FMD and the mean rain area shows maximum along the ITCZ and at higher latitudes around 35°. Indeed, it is confirmed by the study of [30] who compute the distribution of precipitation system size using the Integrated Multi-SatellitE Retrievals for the Global precipitation measurement (IMERG) level 3 gridded product. Their Figure 1 shows that the median precipitation system size is large at latitude above 40°N and 40°S. [21] also displays the geographical distribution of the slope of the RCCD. The corresponding mean diameter of the rain cells is consistent with the previous results over the ITCZ tropics with a value of about 16 km but this value drop to 4 km to 6 km at higher latitudes. Since the rain rate is lower at higher latitude, this difference may be due to a weakness of the approach based on Ku-band measurements, less sensitive to precipitations.

Preprints (www.preprints.org) | NOT PEER-REVIEWED | Posted: 28 September 2021 doi:10.20944/preprints202109.0477.v1

Table 2: Characteristic of rain cells retrieved by the ACECAL approach (global statistics)

Attenuation at peak maximum (Rain rate [mm.h^{-1}] @ 6 km thickness ; 3 km thickness)				
99th percentile	90th percentile	median	10th percentile	1st percentile
0.5 dB (<1 ; <1)	1.0 dB (<1 ; <1)	3.5 dB (1.5 ; 2.4)	13 dB (6 ; 9)	23 dB (10 ; 16)
Rain cell diameter				
99th percentile	90th percentile	median	10th percentile	1st percentile
5 km	8.5 km	15 km	41 km	103 km
Peak diameter (FWHM)				
99th percentile	90th percentile	median	10th percentile	1st percentile
1.5 km	3 km	5 km	10 km	20 km

4. Conclusion

The use of Ka-band for radar altimeter allows a reduction of the spatial resolution from about 15 km with the historical Ku-band instruments to about 4 km. But it also comes with a larger sensitivity to the atmospheric attenuation, especially under rainy conditions.

As the radiometers on-board altimetry mission have a coarser spatial resolution (12 km for MWR on-board SARAL/AltiKa), a new approach is proposed here, based on the 40 Hz σ_0 (one point every 175 m), to characterize the impact of rain cells onto the measurements and anticipate the availability of the observations performed by future two-dimensional swath Ka-band altimeters.

The ACECAL approach combines low-filtering and non-linear fit to retrieve the amplitude of the atmospheric attenuation at Ka-band, the size and the occurrences of rain cells.

The conclusion of this work can be discussed according to two different applications.

First, the robust characterization of rain cells can be used to draw some guidelines for the future altimetry missions. At global scale, the number of observations strongly impacted by the atmospheric attenuation should be limited, with a proportion of observations belonging to attenuation cells lying between 5% and 10%: this result first shown by Tournadre et al. 2015 is confirmed here with a different method. Then, the maximum value of attenuation above which the measurements are no longer valid depends on the signal-to-noise ratio specific to each instrument: according to this limit, the percentage of data availability for a given mission is deduced from the Figure 5 and applying a conservative 10% factor as the percentage of observations inside rain cells at global scale. The Figure 4 provides a declination of this correction factor by bands of latitudes. Generic conclusions can yet be drawn using the geographical distribution of the size and the amplitude: that some regions of particular interest for oceanography as Gulf Stream, North Pacific or Brazil currents could be systematically affected in terms of data availability or degraded budget errors. The present work could also help for two distinct aspects of the altimetry system. First, the distribution of size and amplitude could be used by the prototypes developed in the frame of future swath altimetry missions: added to the simulations of the geophysical context, it could improve the accuracy of the budget errors by including degraded cases caused by the atmosphere and help to the definition of future validation metrics to detect those atmospheric events. Secondly, as the limitation of the current atmospheric attenuation retrieval from radiometer measurements has been illustrated, a potential application of the ACECAL approach is to build a pattern index of atmospheric attenuation from the 40 Hz flagged measurements to be used as a learning database for a future empirical approach based on pattern recognition techniques.

Secondly, this work demonstrates the capability of Ka-band radar altimeter to provide observations strongly consistent to the measurements provided by missions dedicated to the precipitations, as the precipitation radar on-board the TRMM mission. The retrieval of rain rate and rain cell size but also the characterization of the internal peaks, if they are distributed as

secondary products of altimetry missions would certainly benefit to the community, especially if the approach can be generalized to the future two-dimensional swath altimetry missions.

Yet, some aspects of the ACECAL approach could be improved in order to increase its robustness. A first lead would be to assess if there is some interest to apply it independently from existing rain flags: whether ACECAL would provide more robust detections of rain events, minimizing the number of missing events is still to be investigated. A major step would be also to estimate the rain rate from the attenuation provided by this method: the accuracy of the computation of the relative attenuation with respect to the fitted background has to be assessed and the most suitable retrieval method has to be selected. Here again, the validation would benefit from the PEACHI dataset which also contains rain rates match-up from SSMI-S and WindSat missions.

Author Contributions: Methodology and investigations: B.P., N.P and G.D., writing—original draft preparation: B.P.; writing—review and editing: All; supervision: N.P. and G.D.; All authors have read and agreed to the published version of the manuscript.

Funding: This research was funded by CNES

Acknowledgments: Support from CNES for data collection and computing facilities is acknowledged.

Conflicts of Interest: The authors declare no conflict of interest.

References

1. Escudier, P.; Couhert, A.; Mercier, F.; Picard, B. Satellite radar altimetry: principle, accuracy and precision. In *Satellite Altimetry Over Oceans and Land Surfaces*; Press, B.R.C., Ed.; Taylor & Francis Inc, 2018; chapter 1, pp. 1–70.
2. Fu, L.L.; Christensen, E.; Yamarone, C.; Lefebvre, M.; Menard, Y.; Dorrer, M.; Escudier, P. TOPEX/Poseidon mission overview. *Journal of Geophysical Research Atmospheres* **1995**, *99*. doi:10.1029/94JC01761.
3. Heslop, E.E.; Sánchez-Román, A.; Pascual, A.; Rodríguez, D.; Reeve, K.A.; Faugère, Y.; .; Raynal, M. Sentinel-3A Views Ocean Variability More Accurately at Finer Resolution. *Geophys. Res. Lett.* **2017**, *44*, 12367–12374. doi:10.1002/2017GL076244.
4. Quartly, G.D.; Guymer, T.H.; Srokosz, M.A. The Effects of Rain on Topex Radar Altimeter Data. *Journal of Atmospheric and Oceanic Technology* **1996**, *13*, 1209–1229. doi:10.1175/1520-0426(1996)013<1209:TEOROT>2.0.CO;2.
5. Tournadre, J.; Morland, J.C. Effects of rain on TOPEX/Poseidon altimeter data. *IEEE Transactions on Geoscience and Remote Sensing* **1997**, *35*, 1117–1135. doi:10.1109/36.628780.
6. Quartly, G.D. Sea state and rain: A second take on dual-frequency altimetry. *Marine Geodesy* **2004**, *27*, 133–152. doi:10.1080/01490410490465472.
7. Tournadre, J. Validation of Jason and Envisat altimeter dual frequency rain flags. *Marine Geodesy* **2004**, *27*, 153–169. doi:10.1080/01490410490465616.
8. Tran, N.; Obligis, E.; Ferreira, F. Comparison of two Jason-1 altimeter precipitation detection algorithms with rain estimates from the TRMM Microwave Imager. *Journal of Atmospheric and Oceanic Technology* **2005**, *22*, 782–794. doi:10.1175/JTECH1742.1.
9. Steunou, N.; Desjonquères, J.D.; Picot, N.; Sengenes, P.; Noubel, J.; Poisson, J.C. AltiKa Altimeter: Instrument Description and In Flight Performance. *Marine Geodesy* **2015**, *38*, 22–42. doi:10.1080/01490419.2014.988835.
10. Lillibridge, J.; Scharroo, R.; Abdalla, S.; Vandemark, D. One-and two-dimensional wind speed models for ka-band altimetry. *Journal of Atmospheric and Oceanic Technology* **2014**, *31*, 630–638. doi:10.1175/JTECH-D-13-00167.1.
11. Tournadre, J.; Lambin-artru, J.; Steunou, N. Cloud and Rain Effects on AltiKa / SARAL Ka-Band Radar Altimeter — Part I : Modeling and Mean Annual Data Availability. *Science* **2009**, *47*, 1806–1817.
12. Tournadre, J.; Lambin, J.; Steunou, N. Cloud and rain effects on ALTIKA / SARAL Ka band radar altimeter . Part II : Definition of a rain / cloud flag. *IEEE Trans.\ Geosci.\ Remote Sens.* **2009**, *47*, 1–9.
13. Tournadre, J.; Poisson, J.; Steunou, N.; Picard, B. Validation of AltiKa Matching Pursuit Rain Flag. *Marine Geodesy* **2015**, *38*. doi:10.1080/01490419.2014.1001048.
14. Fu, Y.; Chen, Y.; Zhang, X.; Wang, Y.; Li, R.; Liu, Q.; Zhong, L.; Zhang, Q.; Zhang, A. Fundamental Characteristics of Tropical Rain Cell Structures as Measured by TRMM PR. *Journal of Meteorological Research* **2020**, *34*, 1129–1150. doi:10.1007/s13351-020-0035-5.
15. Mesnard, F.; Sauvageot, H. Structural characteristics of rain fields. *Journal of Geophysical Research: Atmospheres* **2003**, *108*, n/a–n/a. doi:10.1029/2002JD002808.
16. Capsoni, C.; Fedi, F.; Magistroni, C.; Paraboni, A.; Pawlina, A. Data and theory for a new model of the horizontal structure of rain cells for propagation applications. *Radio Science* **1987**, *22*, 395–404. doi:10.1029/RS022i003p00395.
17. Sauvageot, H.; Mesnard, F.; Tenório, R.S. The Relation between the Area-Average Rain Rate and the Rain Cell Size Distribution Parameters. *Journal of the Atmospheric Sciences* **1999**, *56*, 57–70. doi:10.1175/1520-0469(1999)056<0057:TRBTAA>2.0.CO;2.
18. Begum, S.; Otung, I.E. Rain cell size distribution inferred from rain gauge and radar data in the UK. *Radio Science* **2009**, *44*, n/a–n/a. doi:10.1029/2008rs003984.
19. Nesbitt, S.W.; Cifelli, R.; Rutledge, S.A. Storm morphology and rainfall characteristics of TRMM precipitation features. *Monthly Weather Review* **2006**, *134*, 2702–2721. doi:10.1175/MWR3200.1.

20. Liu, C.; Zipser, E. Regional variation of morphology of organized convection in the tropics and subtropics. *Journal of Geophysical Research Atmospheres* **2013**, *118*, 453–466. doi:10.1029/2012JD018409.
21. Tournadre, J. Improved level-3 oceanic rainfall retrieval from dual-frequency spaceborne radar altimeter systems. *Journal of Atmospheric and Oceanic Technology* **2006**, *23*, 1131–1149. doi:10.1175/JTECH1897.1.
22. Picard, B.; Frery, M.L.; Obligis, E.; Eymard, L.; Steunou, N.; Picot, N. SARAL/AltiKa Wet Tropospheric Correction: In-Flight Calibration, Retrieval Strategies and Performances. *Marine Geodesy* **2015**, *38*, 277–296. doi:10.1080/01490419.2015.1040903.
23. Valladeau, G.; Thibaut, P.; Picard, B.; Poisson, J.C.; Tran, N.; Picot, N.; Guillot, A. Using SARAL/AltiKa to Improve Ka-band Altimeter Measurements for Coastal Zones, Hydrology and Ice: The PEACHI Prototype. *Marine Geodesy* **2015**, *38*, 124–142. doi:10.1080/01490419.2015.1020176.
24. Vose, R.; Becker, A.; Hilburn, K.; Huffman, G.; Kruk, M.; Yin, X. Precipitation [in "State of the Climate in 2015"]. *Bulletin of the American Meteorological Society* **2016**, *97*, S27 – S28. doi:10.1175/2016BAMSStateoftheClimate.1.
25. Poisson, J.C.; Quartly, G.D.; Kurekin, A.A.; Thibaut, P.; Hoang, D.; Nencioli, F. Development of an ENVISAT altimetry processor providing sea level continuity between open ocean and arctic leads. *IEEE Transactions on Geoscience and Remote Sensing* **2018**, *56*, 5299–5319. doi:10.1109/TGRS.2018.2813061.
26. Tournadre, J. Determination of rain cell characteristics from the analysis of TOPEX altimeter echo waveforms. *Journal of Atmospheric and Oceanic Technology* **1998**, *15*, 387–406. doi:10.1175/1520-0426(1998)015<0387:DORCCF>2.0.CO;2.
27. Newville, M.; Stensitzki, T.; Allen, D.B.; Ingargiola, A. LMFIT: Non-Linear Least-Square Minimization and Curve-Fitting for Python (Version 1.0.1) **2014**. doi:10.5281/zenodo.11813.
28. Goldhirsh, J. Rain Cell Size Statistics as a Function of Rain Rate for Attenuation Modeling. *IEEE Transactions on Antennas and Propagation* **1983**, *31*, 799–801. doi:10.1109/TAP.1983.1143133.
29. Olsen, R.L.; Rogers, D.V.; Hodge, D.B. The aRb Relation in the Calculation of Rain Attenuation. *IEEE Transactions on Antennas and Propagation* **1978**, *26*, 318–329. doi:10.1109/TAP.1978.1141845.
30. Zhang, Y.; Wang, K. Global precipitation system size. *Environmental Research Letters* **2021**, *16*, 054005. doi:10.1088/1748-9326/abf394.